In situ nucleophilic substitutional growth of methylammonium lead iodide polycrystals

Muge Acik,[1,*] Todd M. Alam,[2,#] Fangmin Guo,[3,#] Yang Ren,[3,#] Byeongdu Lee,[3] Richard A. Rosenberg[3], JF Mitchell,[4] Alper Kinaci,[1] Maria Chan,[1] Seth B. Darling[1,5]

[1]Center for Nanoscale Materials, Nanoscience and Technology Division, Argonne National Laboratory, Lemont, IL 60439 USA.

[2]Department of Organic Materials Science, Sandia National Laboratory, Albuquerque, NM 87185 USA.

[3]Advanced Photon Source, X-ray Science Division, Argonne National Laboratory, Lemont, IL 60439 USA.

[4]Materials Science Division, Argonne National Laboratory, Lemont, IL 60439 USA.

[5]Institute for Molecular Engineering, University of Chicago, 5640 South Ellis Avenue, Chicago, Illinois 60637, USA.

*Corresponding author: macik@anl.gov, [#]Equal contribution

Abstract 150 words max

Methylammonium lead iodide ($MAPbI_x$) perovskites are organic-inorganic semiconductors that serve as the light-harvesting component of the photovoltaics, and are desirable with their long diffusion length yielding power conversion efficiencies of ≥22%. Conventional techniques grow perovskites by spin coating precursors on an oxide or a polymer substrate followed by annealing, however, use of high boiling point solvents and high temperatures hinder device stability and performance. Through a one-step, acid-catalyzed nucleophilic-substitutional crystal growth in polar protic solvents, we show evidence for the substrate- and annealing- free production of $MAPbI_x$ polycrystals that are metallic-lead-free with negligibly small amount of PbI_2 precipitation (<10%). On the basis of this chemical composition, we devise an *in situ* growth of highly air (upto ~1.5 months) and thermally-stable (≤300°C), tetragonal-phased, variable-sized polycrystals (~100 nm-10 μm) amendable for large-area deposition, and ultimately, large-scale manufacturing. This method is encouraging for stable optoelectronic devices, and leads to energy-efficient and low-cost processing.

Introduction 3000 words max main text

Methylammonium lead trihalide ($MAPbX_3$) perovskites are favorable due to their unique optical and excitonic properties with variable band gaps, long carrier diffusion length, high absorption coefficient, and low trap-state density to lower energy required for a large-area device fabrication.[1-5] Traditionally, $MAPbX_3$ is grown on an electron/hole transport underlayer with deposition of the precursors dissolved in dimethyl formamide (DMF), dimethyl sulfoxide (DMSO), or gamma butyrolactone (GBL) that is further annealed on a hot plate at 60-200°C,[1,6] via a two-step or a sequential deposition, a toluene dripping, an *in situ* dipping, or a vapor phase deposition method.[7,2,8,9] Nevertheless, these approaches require a substrate and necessitate high temperatures that generate extreme variation in the underlayer film properties with modification of the interfaces by introduction of intrinsic defects, rapid film degradation, and uncontrollable perovskite precipitation.[10] Indeed, excessive heat challenges stoichiometry control in perovskite composition with the presence of halide deficiencies, and leads to an inhomogeneous perovskite crystallization varying over different substrates with an incomplete surface coverage.

To address film morphology, uniformity, stoichiometry, composition, purity issues, and to prevent chemical interfacial reactions due to oxygen-, thermal, or light- induced stability challenges,[11,12] new deposition methods are introduced.[13,14,15] Although these studies improve processes with addition of small molecules, introduction of an excess organic component or treatment with hypophosphorous acid (HPA), following stability challenges arise due to unmanageable surface reactions during perovskite growth. In order to reduce consumption of high boiling solvents and lower reaction temperature, perovskite growth techniques are assisted a single crystal perovskite in an acidic media, particularly studied for the mixed halides of $CH_3NH_3PbI_{3-x}Cl_x$[16] and $(CH_3NH_3)Pb(Br_{1-x}Cl_x)_3$,[17] and a single-halide $MAPbBr_3$ or $MAPbCl_x$[18,19] in DMF from an acid-base colloidal solution,[20] in a HI acid solution,[21] and a Lewis acid-base treatment using different crystallization pathways.[22,23,24,25,26,27] These acid-catalyzed reactions follow a mechanism initiated by the formation of solvated PbI_4^{2-} anions that further react with $CH_3NH_3^+$ cations for $CH_3NH_3PbI_{x(s)}$ growth in solution,[24] where binding sites are determined by varying coordination of solvent ligands.[10] Moreover, purity is reported in these experiments as a devastating challenge due to the use of an ionic liquid scaffold or salt contamination in perovskites. Apparently, $MAPbI_x$ growth with a clear crystallization mechanism in solution remains ambiguous since common growth techniques mostly produce microscopic single crystals assisted by annealing on a substrate. We introduce an *in situ* $MAPbI_x$ growth technique producing highly air-, thermal-, and chemically stable (metallic-lead-free) $MAPbI_x$ that eliminates the use of substrates and annealing. This technique is advantageous over present reports for the use of highly volatile, environmentally benign alcohols, and free from high levels of solvent toxicity as compared to other solvents such as benzene, chloroform, and DMF.

Results and Discussion

***In situ* growth.** We present polar protic anhydrous alcohols (Fig. 1i); such as, methanol, ethanol, 2-propanol, 1-butanol, and 2-butanol assist *in situ* crystallization of $MAPbI_x$ in dispersions (Fig. 1iii). "*In situ"* describes that the crystal growth of $MAPbI_x$ initiates in alcohol dispersions (Fig. 1ii, Fig. S1) by nucleating dark greenish-black polycrystals. Thereafter, a crystal precipitation forms $MAPbI_x$ powders (Fig. S2) upon alcohol evaporation (Fig. S3). This technique therefore suggests a novel alcohol-assisted approach for $MAPbI_x$ without the need of high temperature treatment or a substrate for the perovskite growth that differs from any conventional method. In order to monitor

the crystal orientation and confirm *in situ* growth, we perform high energy synchrotron XRD analysis of $MAPbI_x$ in dispersions (Fig. 2ii). For this purpose, the $MAPbI_x$ dispersions are transferred into quartz capillary tubes sealed in nitrogen at room temperature (Fig. 2i), and then the synchrotron x-ray radiation passes through each of the dispersion. *In situ* high energy XRD (Figs. 2ii-S4) and *in situ* WAXS (Figs. S5-S7) confirm a tetragonal crystal orientation in both dispersion and powders. More specifically, Fig. 2ii presents the peaks at q_z, $(Å)^{-1}$ ~ 1.07, 1.51, 1.78, 1.86, 2.14, 2.39, 2.63, 3.01, and 3.21 $(Å)^{-1}$ corresponding to a tetragonal phase with (110), (200), (211), (202), (004)/(220), (222)/(310), (312), (224), and (411)/(314), respectively. Simulated XRD peaks in Figs. S8-S9 (dispersions) and Figs. S10-S11 (powders) identify the presence of $MAPbI_x$ tetragonal phase for all dispersions and powders, except in toluene having mixed tetragonal-trigonal phases (Fig. S8b). 2D diffraction patterns shown in Fig. S12 confirm the presence of $MAPbI_x$ polycrystals for each of the dispersion. As reported earlier, the existence of peaks below q_z <1 $(Å)^{-1}$ represent intercalation compounds (*i.e.* coordinating species formed at the intermediate steps of the reaction).[28] However, our studies indicate a negligibly small peak at q_z <1.07 $(Å)^{-1}$ associated with a minor PbI_2 precipitation, which represent the efficient alcohol intercalation into the layered PbI_2 structure expanding through the c-axis orientation. Moreover, we perform solid state NMR (ssNMR) (Fig. 3 and Table 1) including solid state ^{1}H, ^{13}C, and ^{207}Pb ssNMR experiments with the $MAPbI_x$ powders which confirm PbI_2 precipitation (<10%) dependent on the reaction efficiency (i.e. binding ability/power of the alcohols)[29] through forming Pb/solvent coordination complexes. Indeed, $MAPbI_x$ polycrystals are found to be metallic-lead-free (i.e. metallic Pb^0) with chemically-stable clean patches as confirmed by Pb4f XPS spectra given in Fig. 2iv for $MAPbI_x$ from 2-propanol, and Fig. S13-S15 for all other alcohols. C1s spectra of $MAPbI_x$ clearly indicate sp^3-C attributed to C-C bonding,[30] and CH_3-NH_3^+ peaks at 285.5 eV and 286.7 eV (Fig. S14), respectively. The negligibly small peak at 288.7 eV is associated with CH_3-NH_2^+ confirming the presence of intercalation compounds (*i.e.* coordinating alcohol molecules).[31]

Mechanism. *In situ* $MAPbI_x$ growth follows a nucleophilic substitution reaction as described in a scheme in Fig. 1ii that determines the efficiency of the crystal growth through the reactivity order of the alcohol binding sites. First, the hydroxyls of alcohols (Fig. 1ii-b_1) are protonated in the acidic environment (pH~ 3-4) due to the presence of highly reactive HI. Next, electron-donor polar protic hydroxyls (-OH) act as the leaving group of the alcohol upon their protonation in the form of hydronium ions (H_3O^+) (Fig. 1ii-b_2), and further interact with the electron pair of the iodide (I^-) - the nucleophile, as methylammonium iodide (CH_3NH_3I) is intercalated into PbI_2. Then, intercalation compounds form (Fig. 1ii-c) within the coordinating alcohol network by the cleavage of H_3O^+/H_2O (Fig. 1ii-b_2). An intermediate C-N bond simultaneously form between the carbon of alcohol and NH_3 of CH_3NH_3I precursor upon a hydroxyl cleavage (i.e. formation of an intercalation compound) (Fig. 1ii-c) that is possibly initiated immediately upon mixing two precursors in alcohols at room temperature. This reaction is catalyzed in an acidic environment (pH ~3-4) initiated with the presence of $HI_{(g)}$ replacing a H atom from NH_3 of MAI - visually observed with a black color change. Thus, a negligible PbI_2 precipitation generates intercalation compounds through the C-N bonds formed between NH_3^+ of the MAI and the carbon of the alcohol that is bound to the methyl groups of methanol, the primary (ethanol, 1-butanol) or a secondary (2-propanol or 2-butanol) hydroxyl (-OH) groups. The C-N bond strength is determined by the easiness of the binding site of the alcohol carbon, following the alcohol reactivity order of methyl<primary<secondary. In other words, the secondary hydroxyls are more easily cleaved than those of primary and methyl alcohols. For instance, 2-propanol and 2-butanol dispersions form stronger C-N bonds of the intercalation compounds relative to those from methanol, ethanol or 1-butanol dispersions.

Therefore, a higher temperature (85°C) is required to cleave C-N in 2-propanol, than methanol (60°C) and ethanol (75°C) or a highly reactive media of 2-butanol is sufficient to cleave the C-N. These intercalation compounds form at the intermediate reaction steps in alcohol dispersions at room temperature that further decompose after heating at the alcohol boiling point up to a 48-hour reaction time. Finally, C-N bonds are replaced with a strong N-H bond (of a NH_3 molecule in MA^+ cations in the perovskite unit cell) as a result of a temperature-assisted growth of $MAPbI_x$ (i.e. *in situ* growth in dispersions). Moreover, highly reactive nature of 1-butanol and 2-butanol allow an immediate crystal formation without the need of heating (Figs. S16). The strong hydrogen bonding in the form of N-H bonds thus result in a thermodynamic energy minimization in addition to the present cation-anion interactions that possibly restrict the molecular rotations (i.e. instability) of the resulting perovskite. $MAPbI_x$ from 1-butanol and 2-butanol dispersions are shown to have similar purity (Figs. S9 - simulated XRD), having a negligibly small PbI_2 fraction lower than 10% in powder form based on our SSNMR analysis (Fig. 3). The conversion efficiency to the perovskite structure is as attributable to the high purity level of the MAI and the PbI_2 precursors, and the efficiency of the stabilized temperature control. The use of anhydrous solvents is yet important to prevent any reactions with the hydroxyl groups of water that hinder perovskite crystal formation and interrupt the N-H bonding, halting the reaction at the intermediate steps.

Characterization. The structural conformation of $MAPbI_x$ is analyzed by Fourier transform infrared attenuated reflectance (FTIR-ATR) spectroscopy with dry powders from (methanol (MeOH, Fig. 2iii-a), ethanol (EtOH, Fig. 2iii-b), 2-propanol (2-PrOH, Fig. 2iii-c), toluene (Fig. 2iii-d), 1-butanol (n-BuOH, Fig. 2iii-e), and 2-butanol (2-BuOH, Fig. 2iii-f) dispersions. The presence of the vibrational modes at ~920 cm^{-1}, ~1485 cm^{-1}, ~1592 cm^{-1}, ~3160 cm^{-1}, and ~3210 cm^{-1} correspond to the presence of C-N stretch, C-H deformation, N-H deformation, C-H stretch, and N-H stretch, respectively, and confirm the perovskite growth.

To gain insights into the conversion and growth yield of $MAPbI_x$, we employ ^1H MAS and ^{13}C MAS NMR analysis (Fig. 3) and the spectra for the isotropic resonance (Figs. S17-S19). The spectra reveal two resonances of an equal integral intensity, consistent with the equivalent number of protons in the NH_3 and CH_3 environments, respectively. These resonances appear at δ = +6.2 ppm (NH_3) and δ = +3.15 ppm (CH_3). The spinning side band patterns (SSB) are found to be identical between different samples demonstrating that there are not any differences in mobility between the different preparations at 295K (305 K corrected for MAS frictional heating). This finding matches the results reported in Baike *et al.,*[32] resulting in a higher quality $MAPbI_x$ with minimal PbI_2 impurity. There are almost no differences in the ^1H environments for these materials except for the perovskite from toluene dispersions, which present a minor impurity and a 2% increase in disorder of the CH_3NH_3 molecules (Fig. S19). All samples show only a single ^{13}C resonance at δ = + 30.1 ppm and are in agreement with ^1H ssNMR findings while perovskites from toluene indicate a second carbon environment, in agreement with the presence of impurities/disorder/domains seen from the ^1H NMR results. The line widths are a bit narrower (more crystalline) showing a high-quality material. In the work of Rosales *et al*.[33] changes in line width are related to the quality of the material disorder and the synthesis. We do not observe this type of variation in our $MAPbI_x$.

In contrast to alcohol dispersions, perovskite conversion efficiency is found to be surprisingly low in toluene dispersions, particularly after toluene removal. Although both *in situ* high energy (Fig. 2ii) and powder (Figs. S20 and S21) XRD analysis represent the peaks highlighting $MAPbI_x$ formed as soon as the precursors are mixed in toluene at room temperature, also visually with a

black color (Fig. 1iii), powder analysis however shows the presence of intercalation compounds with significant PbI_2 precipitation, even for those prepared by heating in toluene at 110°C. The steric effect hinders the efficiency of the $MAPbI_x$ growth in toluene, although the nucleophilic substitution reaction takes place resulting in the cleavage of hydrogen of the CH_3 to bind $CH_3NH_3^+$ as explained in the proposed mechanism in Fig. S22. Although the perovskite growth in toluene follows the same perovskite growth mechanism in all polar alcohols, bulk benzene ring of the toluene confined in the interlayers of PbI_2 induces a steric hindrance and the reaction efficiency, thereby leads to poor perovskite conversion having ~41% of PbI_2 in toluene (from ssNMR spectral fits, Table 1). Moreover, a spectral investigation from solid state ^{207}Pb NMR indicates a fraction of 90, 85, 96, 99, and 89% of methylammonium iodide component, and a PbI_2 fraction of 10, 15, 4, 1, 11% for perovskites from methanol, ethanol, 2-propanol, 1-butanol, and 2-butanol, respectively (Table 1). Among all, 2-propanol and 1-butanol exhibit the most efficient perovskite conversion with a minimum residual of the inorganic component, while toluene leads to the highest fraction of PbI_2 (see optimization in experimental method section and, also Figs. S23-S31). Nevertheless, $MAPbI_x$ growth is not possible in DMF, DMSO, and at <40 wt.% concentrations in alcohols (Figs. S32-35). Therefore, solvent polarity is crucial for $MAPbI_x$ growth.[29]

We find with the SEM analysis that $MAPbI_x$ from methanol dispersions, spin coated from each dispersion on a carbon tape at a large area (Fig. S36-S37) without sonication, have the largest grains (~≤10 μm in Fig. 4i), while their grain size is substantially reduced in all other alcohol dispersions. The crystals obtained from the ethanol dispersion are in a range less than <10 μm (Fig. 4ii), having smaller crystals (<5 μm), mostly ~1 μm, and <500 nm correspond to the crystals from 2-propanol and 1-butanol, respectively (Figs. 4iii and 4iv). The $MAPbI_x$ grains are dominated with the presence of ~200-300 nm from 2-propanol and ~100-300 nm from 1-butanol, much smaller than all other polycrystals. The $MAPbI_x$ is also obtained in the form of platelets from 2-butanol (Fig. 4v) or in a fiber-like morphology from toluene (Fig. 4vi) in their dry powder form. The presence of fiber structure of $MAPbI_x$ from toluene dispersions confirm the large amount of PbI_2. The crystal size of $MAPbI_x$ is thus determined by the alcohol reactivity order. The easiness to bind the alcohol yields a significant reduction of the crystal size from microns to nano scales.

We perform chemical structure and conformation stability tests with infrared spectroscopy and find that the strong N-H bonding in the unit cell of these $MAPbI_x$ yields highly air (Figs. 5i-S38) and thermally stable (Fig. 5ii and Fig. 5iii) polycrystals. In order to perform air stability tests, each perovskite is drop-casted on a Si/SiO_2 substrate, and measurements are done at room temperature in air with uncontrolled humidity levels dried in air in a laboratory chemical hood. Our results emphasize that $MAPbI_x$ deposited on a glass slide in air are stable up to ~1.5 months relative to their initial deposition after solvent removal in nitrogen. $MAPbI_x$ polycrystals are also easy to sonicate in air as tested for 3 hrs. in ethanol (Fig. S26). A color change from black to yellow is visually observed with over a period of 1.5 months (Figs. S39). The presence of both stretch and deformation bonds of C-N (908-960 cm^{-1}), C-H (1471 and ~2800-2950 cm^{-1}) and N-H (1577 and ~3000-3200 cm^{-1}) after ~1.5 months in air reveal highly chemically stable $MAPbI_x$ powders (Fig. S40) from methanol, ethanol and 2-propanol dispersions (Fig. 5i). These polycrystals are found to be redispersable in polar aprotic solvents (hexane, acetone, acetonitrile) and non-polars (toluene), and not stable in alcohols once precipitated (Fig. S41). A hydroxyl network is monitored as a result of adsorbed water from the lab ambient in time as seen with a hydroxyl stretch mode at ~3100 cm^{-1} for a 1.5-month. The weight loss of ~24% ($MAPbI_x$ from methanol), ~26-27% ($MAPbI_x$ from ethanol, 2-propanol, 1-butanol, and 2-butanol), and ~28%

($MAPbI_x$ from toluene) is analyzed by TGA (Fig. 5ii), and also the mechanism of weight loss associated with the organic component of the perovskites is studied at 40-300°C by *in situ* infrared transmission absorption spectroscopy (Fig. 5iii, a-j). The first mass loss at ~225°C is associated with the evaporation of unreacted MAI and/or the organic mass loss of low boiling point compounds. The mass loss is also confirmed in weight percentages from a fast heat analysis (10°C/min. Fig. S42), which highlight the reproducibility and repeatability. As a comparison to Dualeh *et. al*'s TGA studies with $MAPbI_x$, our perovskites are comparably stable with minimal mass loss (~24-28 wt.%) since their study indicates ~20-25 wt.% of mass loss up to 400°C.[34] Nevertheless, different than this study, we do not observe two inner losses at ~85-125°C corresponding to HI and CH_3NH_2 sublimation. The absence of amine loss in our TGA data is because of strong hydrogen bonds formed in $MAPbI_x$ that reveals high quality $MAPbI_x$ in their powder form through *in situ* growth technique without any remaining unreacted by-products such as HI or CH_3NH_2.

The optical properties of $MAPbI_x$ are comparable with the perovskites produced via conventional growth techniques over various substrates, as tested by UV-Vis-NIR reflectance spectra given in Fig. 5iv. Each spectrum is collected using integrated sphere detector with drop casted $MAPbI_x$ on a quartz substrate, and reveal the high reflectivity of each of the $MAPbI_x$ perovskite (~85-90%) obtained from dispersions of methanol, ethanol, 2-propanol, 1-butanol, and 2-butanol (Fig. 5iv, a-f). The reduction in reflectivity of $MAPbI_x$ from toluene (Fig. 5iv-d) to ~75% is attributed to the presence of large amount of PbI_2 and the presence of mixed phases. The optical band gap is similar for all the perovskites (~1.5-1.6 eV), comparable to the $MAPbI_x$ obtained from conventional growth techniques (spin coating of the precursors from DMF followed with an annealing).

Conclusion

We, herein, report a very simple methodology for a tetragonal phase growth of $MAPbI_x$ polycrystals from alcohol dispersions with a high symmetry crystal orientation, initiated by *in situ* nucleophilic substitutional growth reactions. The resulting $MAPbI_x$ through a strong N-H hydrogen bonding are found to be highly air stable (up to 1.5 months) preserving their conformational structure, and also chemical (metallic-lead-free) and thermal stability (up to ~300°C). This breakthrough perovskite growth method will thus open new paths to highly repeatable and reproducible fabrication processes for large-scale deposition of $MAPbI_x$, enhance further investigation for its implementation into different device architectures, and eventually bring opportunities to flexible device manufacturing through inexpensive deposition techniques. These high-quality crystalline perovskites, in both dispersion and powder forms, are therefore at the core of the phenomenal advancement of perovskite optoelectronics that will eventually find their use in photodetectors, optical-thermal sensors, light emitting diodes, light-emitting field-effect transistors, lasers, solar fuels, batteries, supercapacitors, radiation detectors, data storage, hydrogen fuel cells, and photocatalysis.[5]

Experimental Methods 800 words max

***In situ* growth.** Methylammonium iodide (CH_3NH_3I) and lead (II) iodide (PbI_2), from Sigma-Aldrich or Dyesol Inc. (see SI), were introduced at a molar ratio of 1:1 into each anhydrous alcohol (methanol, ethanol, 2-propanol, 1-butanol, 2-butanol, or toluene at a dispersion concentration of 40 wt.%, stirred for 48 hrs. at the boiling points except for 1-butanol and 2-butanol. The solvent was then discarded in nitrogen environment, and further dried in vacuum.

***In situ* synchrotron high energy XRD.** Each $MAPbI_x$ dispersion was transferred into the quartz capillary tubes (1.0 mm OD, 80 mm long, 0.01 mm wall thickness) in a glove box at room temperature, and sealed with epoxy. The measurements were performed at the beamline 11-ID-C at the Advanced Photon Source. A monochromator with a Si (311) single crystal was used to provide an x-ray beam (~105.6 keV, wavelength of 0.117418 Å) with a beam size of 0.5 mm × 0.5 mm for two-dimensional diffraction patterns in the transmission geometry using a Perkin-Elmer detector placed at ~1800 mm away from the sample. Each measurement was calibrated using a standard CeO_2 sample, and converted to 1D patterns using a GSAS-II software.[35]

***In situ* wide angle x-ray scattering.** WAXS data were collected at the beamline 12-ID-B at the Advanced Photon Source. X-ray beam of 14 keV was focused through the dispersions in quartz capillary tubes, and scanned using a XRPad detector (PerkinElmer) positioned at about 0.2 m away from the sample.

Powder XRD. A Bruker D2 Phaser benchtop was operated at a maximum operating power of 30 kV and 10 mA. XRD scans were performed using a coupled θ-2θ mode in the range of 2θ = 5-65° with a count time of 1 s and the step size of 0.02°.

Solid state NMR. The solid state ^{1}H and ^{13}C MAS NMR spectra were acquired by a Bruker Avance – III 600 NMR using a 2.5 mm rotor spinning at 10 kHz using a single pulse Bloch decay with high power ^{1}H decoupling. The ^{13}C NMR chemical shifts were referenced to the secondary external standard adamantane (most upfield reference) δ = +128.5 ppm with respect to TMS = 0.0 ppm. Deconvolutions were obtained using the DMFIT software. The solid state ^{207}Pb MAS NMR analysis was performed by a Bruker Avance – III 400 NMR using a 2.5 mm rotor but in static conditions using the DEPTH background subtraction sequence. The ^{207}Pb chemical shift was set to the secondary external standard $Pb(NO_3)_2$ at δ = -3490 ppm with respect to $Pb(CH_3)_4$ δ = 0.0 ppm.

FTIR. A Thermo Nicolet 670 spectrometer equipped with a KBr beam splitter and a MCT/A detector was used. Each dispersion was spin-coated on a Si/SiO_2 (n-type, CZ, <100> silicon with a 10 nm of thermal oxide), and placed at a ~70° of Brewster's angle with respect to the normal mode. Each spectrum was collected 500 times, and averaged three times to obtain the spectra collected at 600-4000 cm^{-1} with a spectral resolution of 2 cm^{-1}. A Linkam 600 sample stage was combined with the spectrometer for *in situ* studies, equipped with a temperature controller (L-T95-THMS), a computer interface controller, and a chiller. The heating/cooling rate was set at 10°C/min., held for 30 min./T(°C), and the spectrum was collected at 20°C.

Attenuated total reflectance. A Bruker Vertex 70 FTIR spectrometer was equipped with a universal ATR reflection top-plate and a germanium crystal to collect spectra, scanned with a DTGS detector. Each spectrum consisted of 32 spectra, averaged at 400-4000 cm^{-1} with a spectral resolution of 4 cm^{-1}.

Reflectance UV-Vis-NIR. The spectra were collected on a quartz coverslip (1"x1" - 25x25 mm, ~0.2 mm thick, purchased from Electron Microscopy Sciences) at 400-1200 nm by a Perkin Elmer Lambda 950 spectrometer equipped with an integrated sphere detector.

SEM. A JEOL JSM-7500F Field Emission SEM was used to collect the images applying an accelerating voltage of 10 kV and an emission current of 10 μm using a secondary electron detector at a working distance of 6 mm in z-direction.

XPS. XPS measurements were performed in an UHV chamber (base pressure = 2 x 10^{-10} Torr) using a Scienta Omicron Argus electron energy analyzer operating at 20 eV pass energy and a unmonochromatized Al Kα x-ray source. Samples were loaded into a sample introduction chamber and transferred into the analysis chamber, where measurements were made without any further sample treatment. Curve fitting was performed using Casa XPS software.

TGA. Thermogravimetric analysis was carried out on a Mettler-Toledo TGA-DSC1 using 20-50 mg of powder samples loaded into 150 microliter aluminum oxide crucibles, and maintained flowing nitrogen (50 sccm). Samples were heated at 10 °C/min to 150 °C and then at 1 °C/min to 425 °C, holding for 1 hour and then cooled to room temperature at 10 °C/min. Data were corrected for buoyancy effects and baseline drift.

Acknowledgments

This material is based upon work supported by Laboratory Directed Research and Development (LDRD) funding from Argonne National Laboratory, provided by the Director, Office of Science, of the U.S. Department of Energy under Contract No. DE-AC02-06CH11357. Work in the Materials Science Division (thermogravimetric analysis) was supported by the U.S. Department of Energy, Office of Science, Office of Basic Energy Sciences, Materials Science and Engineering Division. MA acknowledges the support from the Joseph Katz Named Fellowship at Argonne National Laboratory, technical support of Peter L. Fuesz and Brandon L. Fisher, and Dr. Kenley Pelzer's fellowship contribution for the equipment support. The NMR portion of the work was performed at Sandia National Laboratories, which is a multi-program laboratory operated by Sandia Corporation, a Lockheed Martin Company, for the United States Department of Energy's National Nuclear Security Administration under Contract DE-AC04-94AL85000.

MA proposed the research idea, performed crystallization experiments, and measurements via spectroscopy, microscopy and powder XRD analysis with data interpretation and derivation of mechanisms, and reported results to SBD. For *in situ* spectroscopy measurements, MA designed a FTIR thermal cell with Peter L. Fisher and Brandon L. Fisher. TMA performed NMR studies and interpreted the data through discussions with MA. BL performed *in situ* WAXS, FG and YR conducted *in situ* high energy XRD experiments. RR analyzed MA's perovskites with XPS. JFM analyzed the samples with TGA, and discussed all the data analysis with MA. MA interpreted all the XRD data with help from BL and YR, and XPS results with RR. All authors reviewed the manuscript and confirmed the authorship contribution to this work.

References

1 Kojima, A., Teshima, K., Shirai, Y. & Miyasaka, T. Organometal Halide Perovskites as Visible-Light Sensitizers for Photovoltaic Cells. *J Am Chem Soc* **131**, 6050-6051, doi:10.1021/ja809598r (2009).

2 Park, N.-G., Grätzel, M., Miyasaka, T., Zhu, K. & Emery, K. Towards stable and commercially available perovskite solar cells. *Nature Energy* **1**, 16152, doi:10.1038/nenergy.2016.152 (2016).

3 Shi, D. *et al.* Low trap-state density and long carrier diffusion in organolead trihalide perovskite single crystals. *Science* **347**, 519-522, doi:10.1126/science.aaa2725 (2015).

4 Stranks, S. D. *et al.* Electron-hole diffusion lengths exceeding 1 micrometer in an organometal trihalide perovskite absorber. *Science* **342**, 341-344, doi:10.1126/science.1243982 (2013).

5 Zhang, W., Eperon, G. E. & Snaith, H. J. Metal halide perovskites for energy applications. *Nature Energy* **1**, 16048, doi:10.1038/nenergy.2016.48 (2016).

6 Nazeeruddin, M. K. & Snaith, H. Methylammonium lead triiodide perovskite solar cells: A new paradigm in photovoltaics. *Mrs Bull* **40**, 641-645, doi:10.1557/mrs.2015.169 (2015).

7 Stranks, S. D., Nayak, P. K., Zhang, W., Stergiopoulos, T. & Snaith, H. J. Formation of Thin Films of Organic–Inorganic Perovskites for High-Efficiency Solar Cells. *Angewandte Chemie International Edition* **54**, 3240-3248, doi:10.1002/anie.201410214 (2015).

8 Sharenko, A. & Toney, M. F. Relationships between Lead Halide Perovskite Thin-Film Fabrication, Morphology, and Performance in Solar Cells. *J Am Chem Soc* **138**, 463-470, doi:10.1021/jacs.5b10723 (2016).

9 Burschka, J. *et al.* Sequential deposition as a route to high-performance perovskite-sensitized solar cells. *Nature* **499**, 316-319, doi:10.1038/nature12340
http://www.nature.com/nature/journal/v499/n7458/abs/nature12340.html#supplementary-information (2013).

10 Manser, J. S., Saidaminov, M. I., Christians, J. A., Bakr, O. M. & Kamat, P. V. Making and Breaking of Lead Halide Perovskites. *Accounts Chem Res* **49**, 330-338, doi:10.1021/acs.accounts.5b00455 (2016).

11 Berhe, T. A. *et al.* Organometal halide perovskite solar cells: degradation and stability. *Energ Environ Sci* **9**, 323-356, doi:10.1039/C5EE02733K (2016).

12 Brunetti, B., Cavallo, C., Ciccioli, A., Gigli, G. & Latini, A. On the Thermal and Thermodynamic (In)Stability of Methylammonium Lead Halide Perovskites. *Sci Rep-Uk* **6**, 31896, doi:10.1038/srep31896
http://www.nature.com/articles/srep31896#supplementary-information (2016).

13 Chen, C.-C. *et al.* One-step, low-temperature deposited perovskite solar cell utilizing small molecule additive. *PHOTOE* **5**, 057405-057405, doi:10.1117/1.JPE.5.057405 (2015).

14 Zhang, W. *et al.* Ultrasmooth organic–inorganic perovskite thin-film formation and crystallization for efficient planar heterojunction solar cells. *Nat Commun* **6**, 6142, doi:10.1038/ncomms7142

http://www.nature.com/articles/ncomms7142#supplementary-information (2015).
15 Zhang, W. *et al.* Enhanced optoelectronic quality of perovskite thin films with hypophosphorous acid for planar heterojunction solar cells. *Nat Commun* **6**, 10030, doi:10.1038/ncomms10030 http://www.nature.com/articles/ncomms10030#supplementary-information (2015).
16 Noel, N. K. *et al.* Enhanced Photoluminescence and Solar Cell Performance via Lewis Base Passivation of Organic–Inorganic Lead Halide Perovskites. *Acs Nano* **8**, 9815-9821, doi:10.1021/nn5036476 (2014).
17 Zhang, T. *et al.* A facile solvothermal growth of single crystal mixed halide perovskite CH3NH3Pb(Br1-xClx)3. *Chem Commun* **51**, 7820-7823, doi:10.1039/C5CC01835H (2015).
18 Yang, Y. *et al.* Low surface recombination velocity in solution-grown CH3NH3PbBr3 perovskite single crystal. *Nat Commun* **6**, 7961, doi:10.1038/ncomms8961 http://www.nature.com/articles/ncomms8961#supplementary-information (2015).
19 Maculan, G. *et al.* CH3NH3PbCl3 Single Crystals: Inverse Temperature Crystallization and Visible-Blind UV-Photodetector. *The Journal of Physical Chemistry Letters* **6**, 3781-3786, doi:10.1021/acs.jpclett.5b01666 (2015).
20 Nayak, P. K. *et al.* Mechanism for rapid growth of organic–inorganic halide perovskite crystals. *Nat Commun* **7**, 13303, doi:10.1038/ncomms13303 http://www.nature.com/articles/ncomms13303#supplementary-information (2016).
21 Dang, Y. *et al.* Bulk crystal growth of hybrid perovskite material CH3NH3PbI3. *Crystengcomm* **17**, 665-670, doi:10.1039/C4CE02106A (2015).
22 Saidaminov, M. I. *et al.* High-quality bulk hybrid perovskite single crystals within minutes by inverse temperature crystallization. *Nat Commun* **6**, 7586, doi:10.1038/ncomms8586 http://www.nature.com/articles/ncomms8586#supplementary-information (2015).
23 Peng, W. *et al.* Solution-Grown Monocrystalline Hybrid Perovskite Films for Hole-Transporter-Free Solar Cells. *Adv Mater* **28**, 3383-3390, doi:10.1002/adma.201506292 (2016).
24 Fu, Y. *et al.* Solution Growth of Single Crystal Methylammonium Lead Halide Perovskite Nanostructures for Optoelectronic and Photovoltaic Applications. *J Am Chem Soc* **137**, 5810-5818, doi:10.1021/jacs.5b02651 (2015).
25 Tian, W., Zhao, C., Leng, J., Cui, R. & Jin, S. Visualizing Carrier Diffusion in Individual Single-Crystal Organolead Halide Perovskite Nanowires and Nanoplates. *J Am Chem Soc* **137**, 12458-12461, doi:10.1021/jacs.5b08045 (2015).
26 Moore, D. T. *et al.* Direct Crystallization Route to Methylammonium Lead Iodide Perovskite from an Ionic Liquid. *Chem Mater* **27**, 3197-3199, doi:10.1021/cm5047484 (2015).
27 Liang, K., Mitzi, D. B. & Prikas, M. T. Synthesis and Characterization of Organic–Inorganic Perovskite Thin Films Prepared Using a Versatile Two-Step Dipping Technique. *Chem Mater* **10**, 403-411, doi:10.1021/cm970568f (1998).
28 Jeon, N. J. *et al.* Solvent engineering for high-performance inorganic-organic hybrid perovskite solar cells. *Nat Mater* **13**, 897-903, doi:10.1038/nmat4014 (2014).
29 Stevenson, J. *et al.* Mayer Bond Order as a Metric of Complexation Effectiveness in Lead Halide Perovskite Solutions. *Chem Mater*, doi:10.1021/acs.chemmater.6b04327 (2016).
30 Liu, L., E-mail: ljliu@suda.edu.cn, E-mail: jmcleod@suda.edu.cn, McLeod, J. A., E-mail: ljliu@suda.edu.cn, E-mail: jmcleod@suda.edu.cn, Wang, R., Shen, P. & Duhm, S. Tracking the formation of methylammonium lead triiodide perovskite. *Appl Phys Lett*, Medium: X; Size: page(s) 061904-061904.061905 (2015).
31 Calloni, A. *et al.* Stability of Organic Cations in Solution-Processed CH3NH3PbI3 Perovskites: Formation of Modified Surface Layers. *The Journal of Physical Chemistry C* **119**, 21329-21335, doi:10.1021/acs.jpcc.5b05422 (2015).

32 Baikie, T. *et al.* A combined single crystal neutron/X-ray diffraction and solid-state nuclear magnetic resonance study of the hybrid perovskites CH3NH3PbX3 (X = I, Br and Cl). *Journal of Materials Chemistry A* **3**, 9298-9307, doi:10.1039/C5TA01125F (2015).
33 Rosales, B. A. *et al.* Persistent Dopants and Phase Segregation in Organolead Mixed-Halide Perovskites. *Chemistry of Materials*, doi:10.1021/acs.chemmater.6b01874 (2016).
34 Dualeh, A., Gao, P., Seok, S. I., Nazeeruddin, M. K. & Grätzel, M. Thermal Behavior of Methylammonium Lead-Trihalide Perovskite Photovoltaic Light Harvesters. *Chem Mater* **26**, 6160-6164, doi:10.1021/cm502468k (2014).
35 Toby, B. H. & Von Dreele, R. B. GSAS-II: the genesis of a modern open-source all purpose crystallography software package. *Journal of Applied Crystallography* **46**, 544-549, doi:10.1107/S0021889813003531 (2013).

Figures

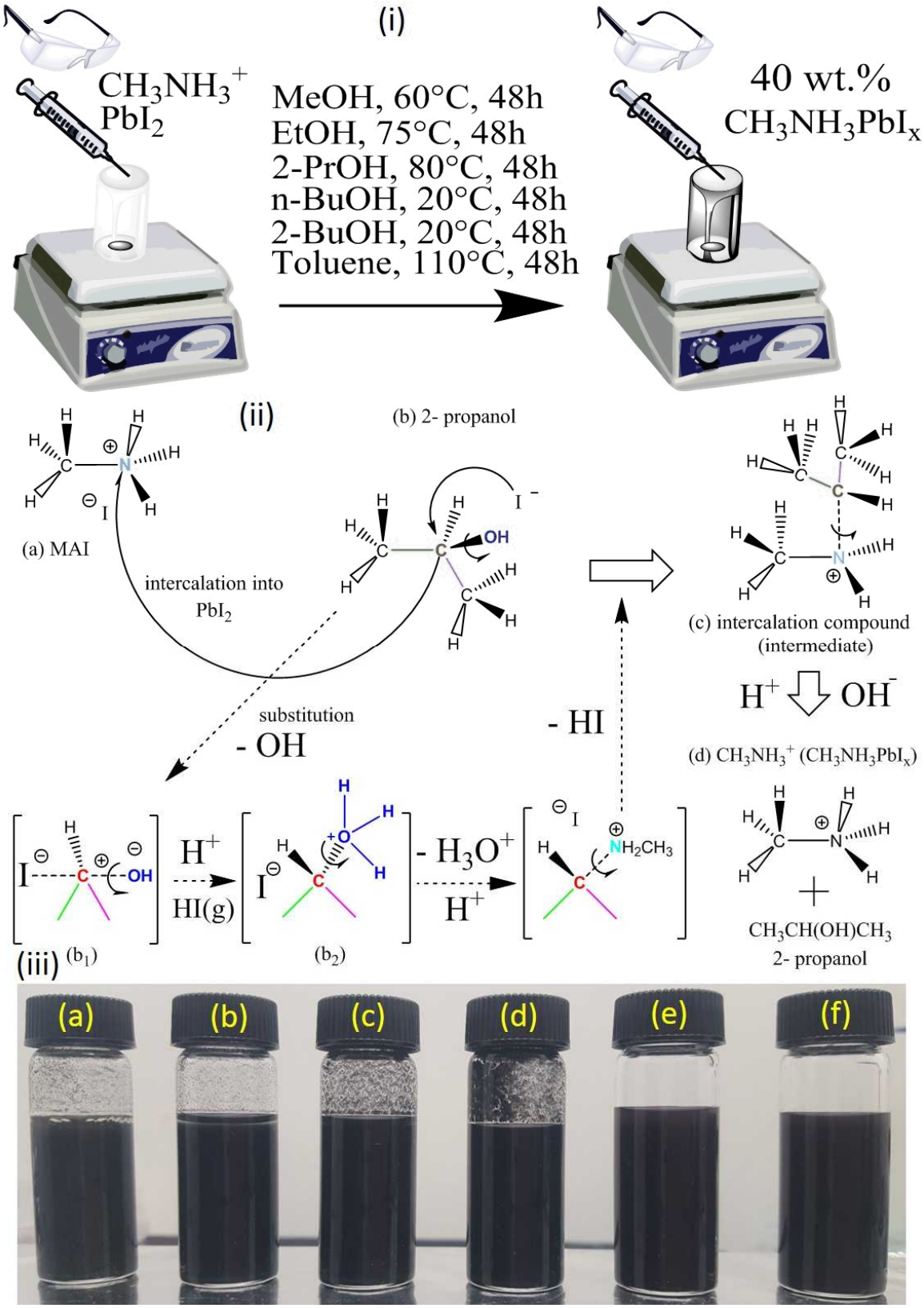
(i)
$CH_3NH_3^+$
PbI_2
MeOH, 60°C, 48h
EtOH, 75°C, 48h
2-PrOH, 80°C, 48h
n-BuOH, 20°C, 48h
2-BuOH, 20°C, 48h
Toluene, 110°C, 48h
40 wt.%
$CH_3NH_3PbI_x$
(ii)
(a) MAI
(b) 2- propanol
intercalation into PbI_2
(c) intercalation compound (intermediate)
substitution
- OH
- HI
H^+ OH^-
(d) $CH_3NH_3^+$ ($CH_3NH_3PbI_x$)
H^+
HI(g)
- H_3O^+
H^+
(iii) (b_1)
(b_2)
$CH_3CH(OH)CH_3$
2- propanol
(a)
(b)
(c)
(d)
(e)
(f)

Figure 1. (i) Schematic representation of experimental set-up: Mixing methylammonium iodide (CH_3NH_3I) with lead (II) iodide (PbI_2) at a solution concentration of 40 wt.% in methanol (60°C), ethanol (75°C), 2-propanol (80°C), 1-butanol (20°C), 2-butanol (20°C) or in toluene (110°C), stirred continuously at the solvent boiling point for 48 hrs in nitrogen environment. Mechanisms for one-step *in situ* MAPbIx perovskite growth in 2-propanol. Nucleophilic substitution with a halide (iodide) attack in the presence of electron donating leaving groups (hydroxyls in alcohols – strongly activating) or (hydrogen from CH_3 of toluene – weakly activating) of the solvent, shown for methylammonium iodide (CH_3NH_3I) mixed with lead (II) iodide (PbI_2) leading to the formation of methylammonium cations ($CH_3NH_3^+$) in the unit cell of $CH_3NH_3PbI_x$. (iv) Methylammonium lead iodide ($MAPbI_x$) dispersions in (a) methanol, (b) ethanol, (c) 2-propanol, (d) toluene, (e) 1-butanol, and (f) 2-butanol, prepared at the solvent boiling point, and further cooled down to room temperature.

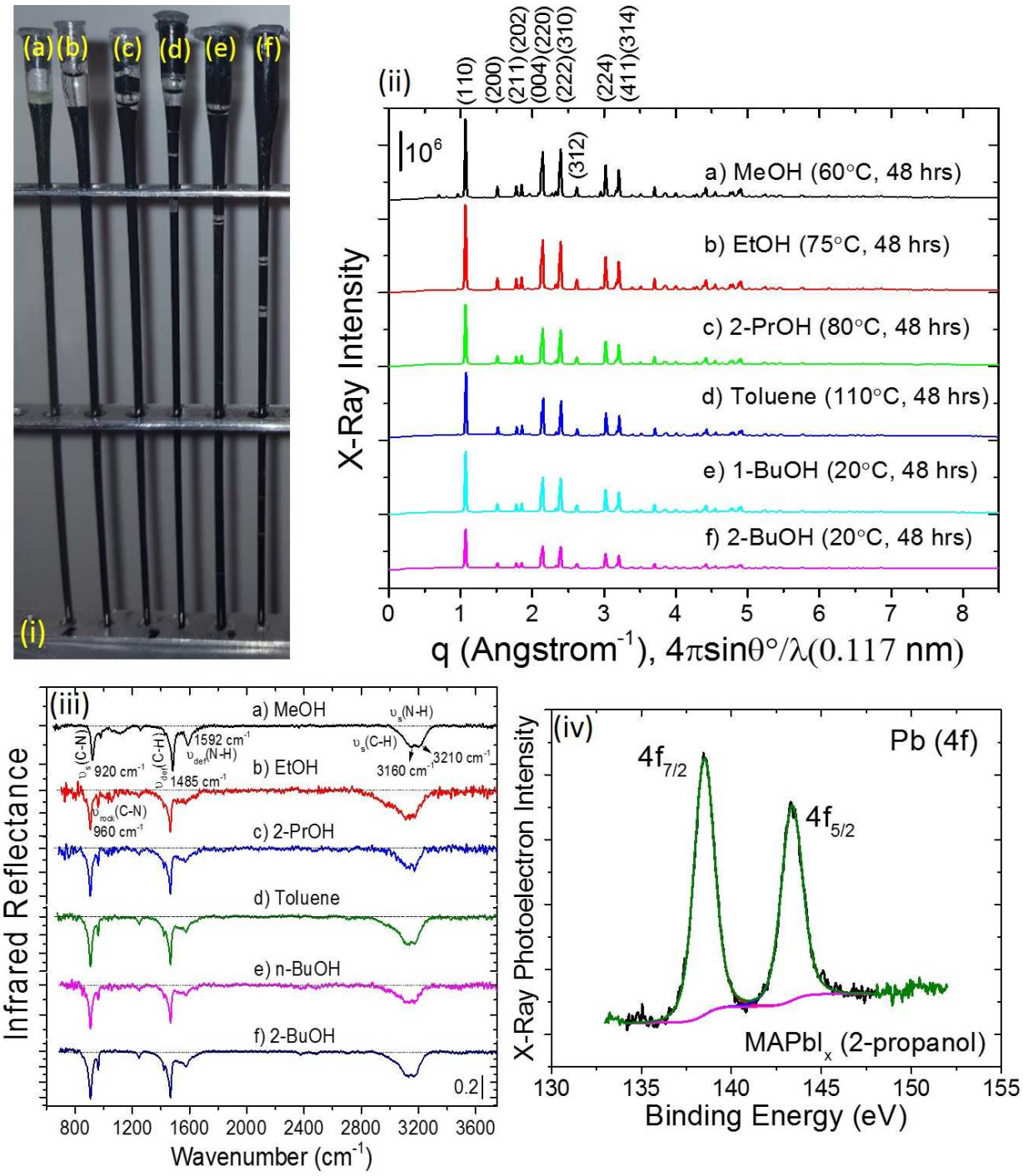

Figure 2. (i) Methylammonium lead iodide ($CH_3NH_3PbI_x$) dispersed in the form of black crystals in (a) methanol, (b) ethanol, (c) 2-propanol, (d) toluene, (e) 1-butanol, and (f) 2-butanol, respectively, filled in the quartz capillary tubes, and sealed with epoxy. (ii) *In situ* (in solution) high energy synchrotron XRD analysis for the crystallographic orientation of crystals, prepared in (a) methanol, (b) ethanol, (c) 2-propanol, (d) toluene, (e) 1-butanol, and (f) 2-butanol. q=4*pi*sin(theta)/lambda, where lambda = 0.117 nm. (iii) FTIR-ATR reflectance (%R) spectra of $MAPbI_x$ powders at room temperature in air, grown in (a) methanol (60°C, 48hrs), (b) ethanol (75°C, 48hrs), (c) 2-propanol (80°C, 48hrs), (d) toluene (110°C, 48hrs), (e) 1-butanol (20°C,

48hrs), and (f) 2-butanol (20°C, 48hrs). (iv) X-ray photoelectron spectrum of Pb (4f) for the $CH_3NH_3PbI_x$ drop-casted from a 2-propanol dispersion over a tantalum substrate, and further vacuum dried.

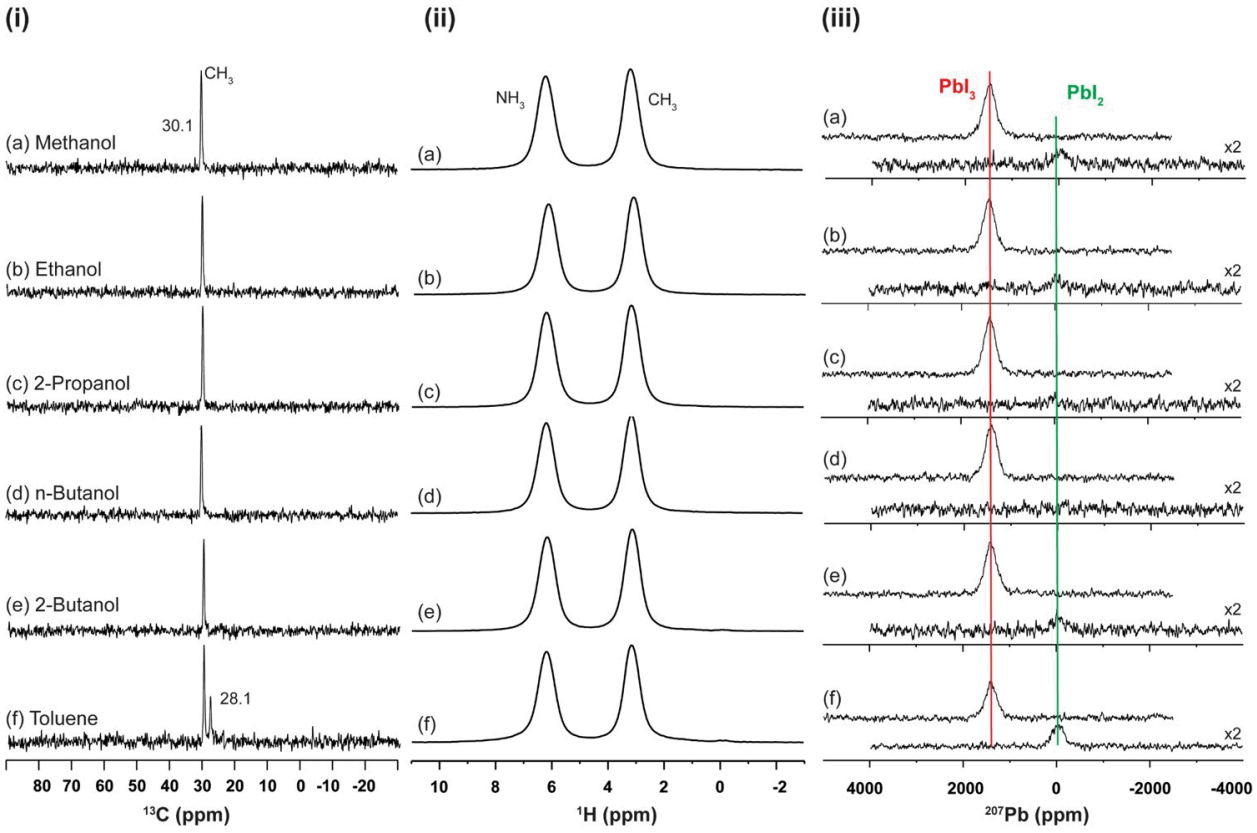

Figure 3. Solid state ^{13}C (i) and ^{1}H NMR analysis (ii) of methylammonium lead iodide ($CH_3NH_3PbI_3$), prepared in (a) methanol, (b) ethanol, (c) 2-propanol, (d) n-butanol, (e)2-butanol, and (f)toluene, respectively (top to bottom). (iii) ^{207}Pb NMR of methylammonium lead iodide with the individual spectrum centered at the proposed PbI_3 and PbI_2 chemical shift for (a) ethanol, (b) toluene, (c) 2-propanol, (d) methanol, (e) 2-butanol, and (f) 1-butanol.

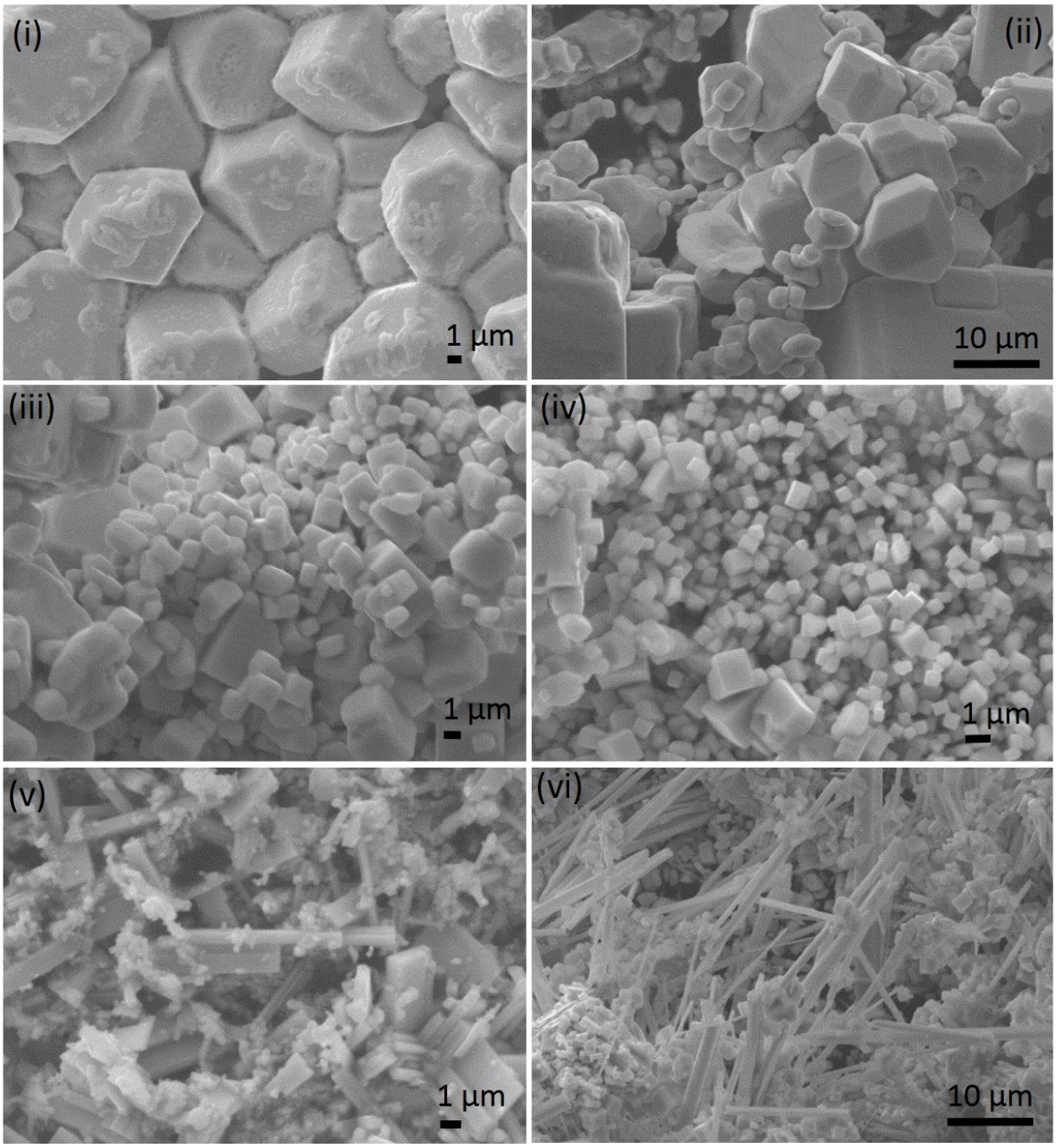

Figure 4. SEM images of methylammonium lead iodide ($CH_3NH_3PbI_x$) powders precipitated from (i) methanol, (ii) ethanol, (iii) 2-propanol, (iv) 1-butanol, (v) 2-butanol, and (v) toluene, respectively. Each dispersion was spin-coated on a carbon tape to capture these images.

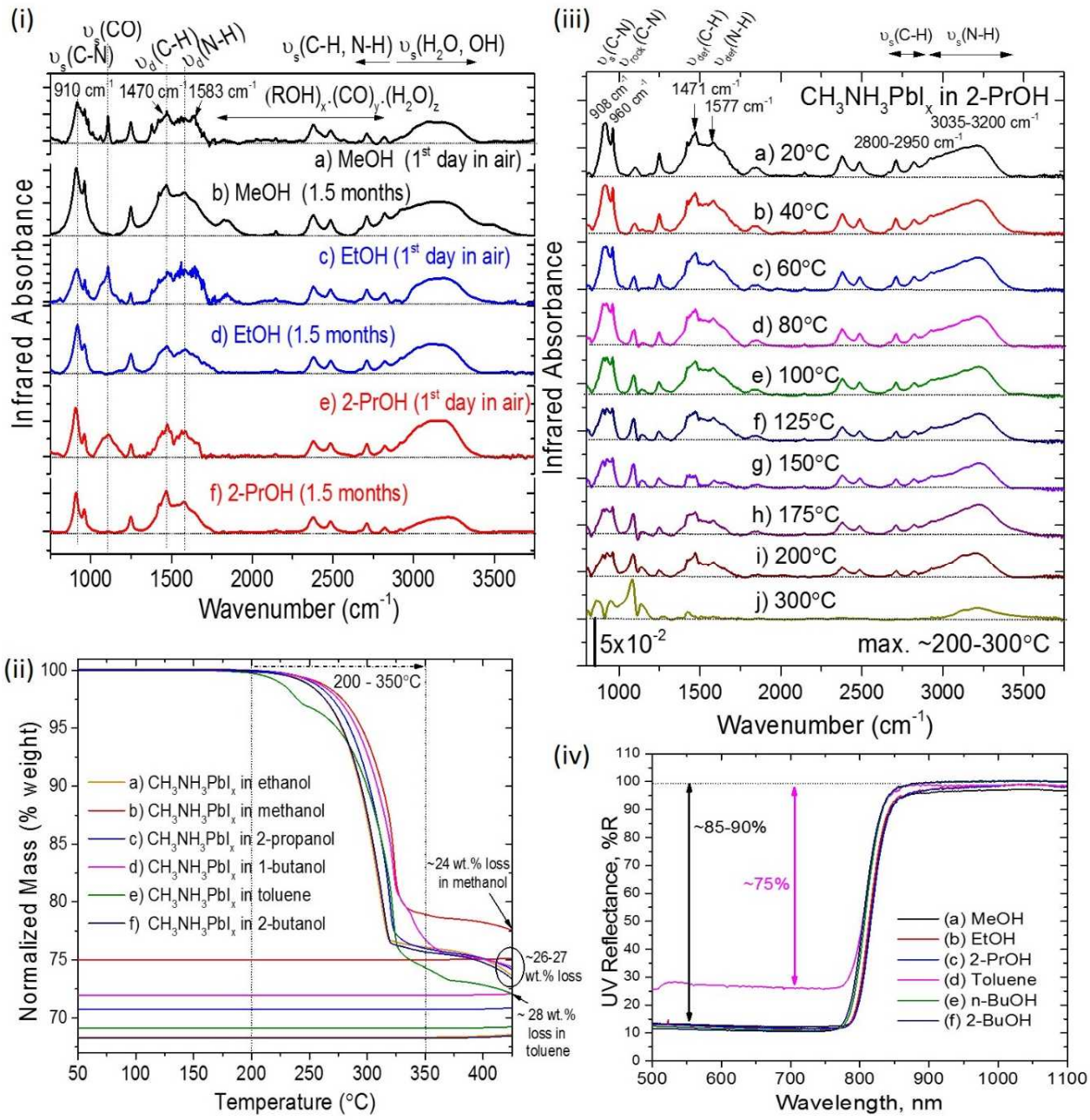

Figure 5. (i) Infrared transmission absorbance spectra of spin-coated $MAPbI_x$ in (a-b) methanol, (c-d) ethanol, (e-f) 2-propanol for initial deposition and after 2 months in air. (ii) Thermogravimetric analysis of $CH_3NH_3PbI_x$ powders, derived from dispersions in (a) methanol, (b) ethanol, (c) 2-propanol, (d) 1-butanol, (e) 2-butanol, and (f) toluene. (iii) *In situ* transmission infrared absorbance spectra of the spin-coated $MAPbI_x$ on a Si/SiO_2 substrate at room temperature (a), further annealed at 40-300°C in argon (b-j). Each spectrum is referenced to the initial Si/SiO_2 spectrum collected at room temperature. The vibrational modes of C-N stretch at 908 cm^{-1}, C-N rocking at 960 cm^{-1}, C-H deformation at 1471 cm^{-1}, C-H stretch at 2800-2950 cm^{-1}, N-H deformation at 1577 cm^{-1}, and N-H stretch at 3035-3200 cm^{-1} are shown on top of the infrared spectra. (iv) UV-Vis-NIR (diffuse reflectance with integrated sphere, %R) of $MAPbI_x$ powders at room temperature in

air, grown in (a) methanol (60°C, 48hrs), (b) ethanol (75°C, 48hrs), (c) 2-propanol (80°C, 48hrs), (d) toluene (110°C, 48hrs), (e) 1-butanol (20°C, 48hrs), and (f) 2-butanol (20°C, 48hrs).

Table 1. Summary of ^{207}Pb NMR spectral parameters

Sample	$CH_3NH_3PbI_3$			PbI_2		
	δ (ppm)	FWHM (kHz) [FWHM (ppm)]	Fraction (%)	δ (ppm)	FWHM (Hz) [FWHM (ppm)]	Fraction (%)
Methanol	1415±5	26.6 [318]	90	Fixed	Fixed	10
Ethanol	1413±5	24.6 [293]	85	Fixed	Fixed	15
2-Propanol	1416±5	25.2 [300]	96	Fixed	Fixed	4
1-Butanol	1434±5	24.9 [298]	99	Fixed	Fixed	1
2-Butanol	1414±5	25.5 [305]	89	Fixed	Fixed	11
Toluene	1416±5	25.6 [306]	59	-32.7	25.6 [305]	41